



# Radiation shielding features for various tellurium-based alloys: a comparative study

M. H. A. Mhareb<sup>1,2,\*</sup>, Mostafa Zeama<sup>3</sup>, Mohamed Elsafi<sup>4</sup>, Y. S. Alajerami<sup>5</sup>, M. I. Sayyed<sup>6,7</sup>, Gameel Saleh<sup>8</sup>, R. M. Hamad<sup>3</sup>, and M. Kh. Hamad<sup>9,\*</sup>

<sup>1</sup>Department of Physics, College of Science, Imam Abdulrahman Bin Faisal University, P.O. Box 1982, Dammam 31441, Saudi Arabia

<sup>2</sup>Basic and Applied Scientific Research Center, Imam Abdulrahman Bin Faisal University, P.O. Box 1982, Dammam 31441, Saudi Arabia

<sup>3</sup>Physics Department, King Fahd University of Petroleum & Minerals, Dhahran 31261, Saudi Arabia

<sup>4</sup>Physics Department, Faculty of Science, Alexandria University, Alexandria 21511, Egypt

<sup>5</sup>Medical Imaging Department, Applied Medical Sciences Faculty, Al Azhar University-Gaza, Gaza City, Palestine

<sup>6</sup>Department of Physics, Faculty of Science, Isra University, Amman, Jordan

<sup>7</sup>Department of Nuclear Medicine Research, Institute for Research and Medical Consultations (IRMC), Imam Abdulrahman Bin Faisal University (IAU), P.O. Box 1982, Dammam 31441, Saudi Arabia

<sup>8</sup>Department of Biomedical Engineering, College of Engineering, Imam Abdulrahman Bin Faisal University, P.O. Box 1982, Dammam, Saudi Arabia

<sup>9</sup>Department of Basic Sciences, School of Social and Basics Sciences, Al Hussein Technical University, Amman, Jordan

**Received:** 21 June 2021

**Accepted:** 16 September 2021

**Published online:**

25 September 2021

© The Author(s), under exclusive licence to Springer Science+Business Media, LLC, part of Springer Nature 2021

## ABSTRACT

We investigate the radiation shielding properties for four Te-based alloys. X-ray diffraction patterns revealed pure phases in all studied samples; however, a secondary phase is detected in the CrTe sample in good agreement with the literature. All samples' densities were measured using the Archimedes principle. The mass attenuation coefficient (MAC) was calculated using Geant4 MC Toolkit and then compared with the XCOM data. Many photon-shielding properties were computed for all investigated samples based on the MAC. The Phy-X and SRIM were used to determine the fast neutron removal cross-section ( $\Sigma_R$ ) and projected range, respectively. As a result, PbTe shows superior shielding features compared to the rest of the investigated samples to use this sample in different shielding applications.

Address correspondence to E-mail: mhsabumhareb@iau.edu.sa; hamad\_morad85@yahoo.com

## 1 Introduction

The shielding materials are essential to protect human beings from the biological effects of ionizing radiations such as X-rays and Gamma-rays in CT/PET/SPECT/ imaging rooms and nuclear stations. The proper materials for shielding against a specific range of radiation energy are specified based on their radiation shielding capacities. The lead (Pb), for example, has high atomic number material, high electron density, and hence has high gamma ray's attenuation coefficients. These properties make the materials superior for shielding in medical and industrial applications. The modified concrete [1–3], multilayered materials [4, 5], composite materials [6], polymers [7, 8], glasses [9–13], and ceramics [14–19] have been introduced to use as radiation shielding materials. The use of metallic alloys as an alternative protective shielding material has attracted a lot of attention due to the imperfections of conventional shielding materials. Nickel (Ni) is a ferromagnetic substance used for alloying due to its good nuclear shield design properties for Gamma radiation [20]. Ni-based alloys with different weight fractions (60–80%) of Ni have been investigated [21, 22]. The measured effective atomic number of the introduced alloys showed constant values independent of the applied energy region (30–600 keV). One of the good candidates for the radiation shielding materials is the Inconel 738 alloy with Ni as a significant constituent of 61.5% and twelve other elements of different compositions [23]. It shows an apparent reduction in the effective atomic number ( $Z_{\text{eff}}$ ), mass attenuation coefficient (MAC), and electron density ( $N_{\text{eff}}$ ) when the Compton scattering technique was used with energy in the range of 100–600 keV. It has been observed that increasing the Ni concentration “ $x$ ” of the  $\text{Ni}_x\text{Cr}_{1-x}$  alloy increases the  $Z_{\text{eff}}$  and MAC while decreases the  $K_{\beta}/K_{\alpha}$  intensity ratio value [24]. Some lead (Pb) based alloys have been investigated [25, 26]. The backscattering method was used for  $\text{Pb}_{80}\text{Sn}_{20}$  binary alloy at 662 keV [25]. It shows an inverse relationship between  $Z_{\text{eff}}$  and backscattered counts. Kaur et al. calculated the exposure build-up factor,  $Z_{\text{eff}}$  and  $N_{\text{eff}}$  at (15 keV to 15 MeV), the  $\text{Pb}_{90}\text{Sn}_{10}$  alloy has good radiation shielding properties with a density of  $9.63 \text{ g/cm}^3$  [26]. The radiation shielding capacities of Tungsten (W)-based alloys have been early studied according to their good properties such as hardness,  $Z_{\text{eff}}$ , and high density. Kobayashi et al.

[27] reported that  $\text{W}_{98}\text{Cu}_{1.5}\text{Ni}_{0.5}$  alloy revealed a high density up to  $14 \text{ g/cm}^3$ . The Tungsten carbide has been tested and compared to prove its efficacy for radiation shielding in nuclear medicine [28]. Results showed that when tungsten carbide discs of different thicknesses were exposed to different energies, a lower half-value layer (HVL) and mean free path (MFP) were observed compared with lead discs having the same thickness at the same energies. The different research groups have measured the  $Z_{\text{eff}}$  of  $\text{W}_{65}\text{Cu}_{35}$  alloys at different energies in the range (60–1400) keV. Results showed that the effective atomic number is independent of the energy applied, and the alloy  $\text{W}_{65}\text{Cu}_{45}$  revealed the highest mass attenuation coefficients compared to the others [29, 30]. Copper (Cu)-based alloys are used in different applications because they have high electric and thermal conductivity, strength, and corrosion resistance. CoCuNi alloys have been introduced by Seven et al. in 2004. They observed a photoelectric absorption edge and measured this alloy's MAC in discrete energies ranging from 11.88 to 26 keV [31]. The effect of varying the percentage weight of Ni in the CoCuNi alloy on the  $Z_{\text{eff}}$  numbers was examined by Icelli et al. [32]. They observed no change in the radiation properties when different concentrations of Ni were used in the energy range 15.746–40.930 keV. The Ni was replaced with Ag in the above Cu-based alloy by Apaydin et al., [33]. It was addressed that the new alloy ( $\text{Co}_{36}\text{Cu}_{63.6}\text{Ag}_{0.4}$ ) has better radiation shielding. Kaewkhao et al. studied the shielding properties for  $\text{Cu}_{65.53}\text{Zn}_{34.47}$  alloy at different photon energies; the  $Z_{\text{eff}}$  did not show any change while the MFP increased with increasing the energy [34]. In contrast, another study has been done by Kaewkhao et al. for Cu-based alloy  $\text{Cu}_{57.61}\text{Zn}_{27.59}\text{Ag}_{14.8}$ ; this alloy has a lower melting point, more absorption ability, and lighter weight than lead [23]. Singh et al. introduced the  $\text{Cu}_{66}\text{Ni}_{30}\text{Mn}_2\text{Fe}_2$  compound as a suitable shielding alloy against Gamma rays of energy ranging between 2 and 12 MeV [35]. Iron (Fe)-based alloys gained their merits in shielding from their high strength and corrosion resistance. For nuclear waste storage, Blink et al. proposed a Fe-based alloy with 14 wt% Boron for neutrons absorption [36]. The HVL, MFP,  $N_{\text{eff}}$ , and  $Z_{\text{eff}}$  shielding parameters of steel alloys have been measured by Al-Jaff [37]. This work showed that HVL and MFP are directly proportional to photon energy and inversely proportional to electron density. On the other hand,

MAC and  $Z_{\text{eff}}$  showed dependency on photon energies applied, while  $N_{\text{eff}}$  did not depend on energy. The density of Fe-based alloy (type 304) in the last work reached  $7.9 \text{ g/cm}^3$ . Iron and steel slag alloys with 39.44% of Fe and different compositions of Cl, O, Mg, Al, Si, Ca, Cr, and Mn revealed better gamma-ray shielding properties than pure fly ash [38]. Five iron-based alloys were prepared and tested by Hamad et al. [39]. Results showed that the  $\text{Fe}_{0.95}\text{-Se}_{0.5}\text{Te}_{0.5}$  alloy has an excellent shielding property compared to those with higher concentrations. Chalcogenide alloys are widely used in infrared transmission, semiconductors, photo-voltaic, and phase change optical recording technology applications. As a result, Chalcogenide alloys received significant attention. For instance, Te-based alloys such as GeTe exhibit high thermal stability of the amorphous and fast crystallization times required for the direct optical overwrite process. It can be used as an electrical switch in memory devices like CDs and/or DVDs. This material has high piezoelectricity, which makes it applicable in many different applications. On the other hand, chromium telluride (CrTe) is a ferromagnetic (FM) material with a critical temperature  $T_c$  of about 340 K with nickel-arsenide (NiAs)-type structures [40–42]. At room temperature, the stoichiometric bulk CrTe structure does not exist in the pure hexagonal phase [43].

This article uses the Geant4 MC toolkit, XCOM, Phy-X, and SRIM program [44, 45] to investigate the radiation shielding properties for different Te-based chalcogenide alloys. Many radiation shielding parameters were calculated, such as the mass attenuation coefficient (MAC), effective atomic number ( $Z_{\text{eff}}$ ), effective electron density ( $N_{\text{eff}}$ ), half-value layer (HVL), mean free path (MFP), exposure build-up factor (EBF), energy absorption build-up factor (EABF), the specific absorbed fraction of the energy (SAFE), fast removal cross-section ( $\Sigma_R$ ), and the projected range.

## 2 Materials and methods

### 2.1 Samples preparation and characterization

All investigated alloys were prepared using the conventional solid-state reaction. Stoichiometric ratios of high purity (4 N to 5 N) powders (Pb, Sn,

Ge, Cr, and Te) were used to prepare the samples (see Table 1). The powders were mixed and ground for about 30 min, then pressed into pellets. The pellets were encapsulated in evacuated quartz tubes partially filled with high purity Argon gas. For PbTe, SnTe, and GeTe, a tube furnace is used to melt the sample at  $800 \text{ }^\circ\text{C}$ . The samples were kept at  $800 \text{ }^\circ\text{C}$  for 24 h. After that, the samples were left to cool down slowly for 24 h. The CrTe sample, on the other hand, was gradually heated to  $800 \text{ }^\circ\text{C}$  and annealed for 10 h. The samples were re-powdered, pressed then reannealed at  $1000 \text{ }^\circ\text{C}$  for 24 h. The detail of the preparation method for the CrTe sample is reported elsewhere [40]. Bruker X-ray diffractometer D2-Phaser with  $\text{Cu K}\alpha$  ( $\lambda = 1.54056 \text{ \AA}$ ) has been used to obtain the powdered XRD patterns over  $20^\circ\text{--}80^\circ$ . We used Rietveld refinements available in FULLPROF software to analyze the XRD pattern of CrTe.

The density is an essential parameter in the radiation shielding field because it helps determine the linear attenuation coefficient (LAC). In this study, alloy samples' densities were measured using the Archimedes principle, while the distilled water was employed as immersion fluid. This setup was illustrated in previous works [39].

## 3 Geant4 simulation

We use the Geant4 MC toolkit to investigate the radiation shielding properties of the studied alloys. Geant4 is a toolkit for simulating the passage of particles through matter based on the Monte Carlo method [46, 47]. The simulated setup allows testing different shielding properties of different samples (single, composite, or even multi-layer materials) before studying them experimentally. The simulation contains the detector, the photon source, lead collimator, and the shielding materials in the main volume. The detector of 3 cm radius and 5 cm height is simulated in the z-axis with a cylindrical NaI crystal. The absorbed alloy samples were simulated with proper thicknesses according to the beam energy. The incident beam was collimated using a lead collimator. The beam energy was varied from 0.015 to 15 MeV. The physical processes such as photoelectric, Compton, and pair production interactions were considered. As a result, several parameters of radiation shielding were calculated for the investigated alloy samples (Fig. 1).

**Table 1** Composition ratio for all alloy samples

Sample ID	Molecular weight (g/mol)	Mass (g)					Density (g/cm <sup>3</sup> )
		Cr	Ge	Sn	Pb	Te	
CrTe	179	0.2895				0.7105	3.4075
GeTe	200		0.3627			0.6373	4.7478
SnTe	246			0.4820		0.5180	5.2323
PbTe	334				0.6189	0.3811	6.8615

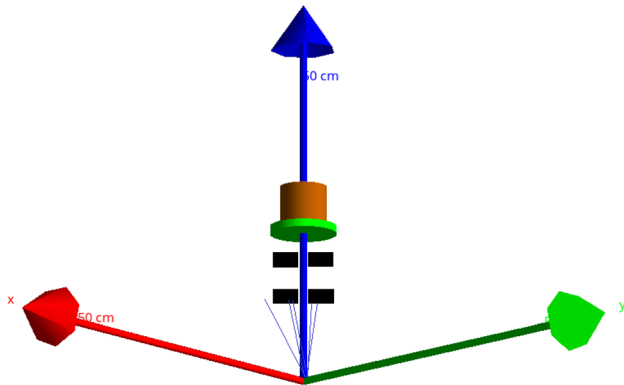


**Fig. 1** Geant4 simulation geometry sketch used in this research

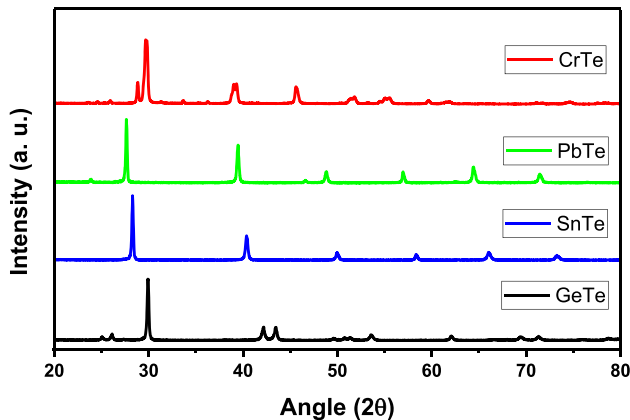


**Fig. 2** X-ray diffraction patterns for CrTe, PbTe, SnTe, and GeTe samples

## 4 Results and discussions

### 4.1 X-ray diffraction (XRD)

XRD was used to confirm the successful preparation of the materials. The data are presented in Fig. 2. The XRD shows that the prepared materials are pure phase with no traces of any impurities. However, a secondary phase was detected in CrTe sample. The

presence of the secondary phase is in good agreement with Steer et al. [48]. According to Street et al., CrTe exists over a range of stoichiometry with the hexagonal NiAs structure. It is worth mentioning that even after the second prolonged annealing, the pure CrTe sample was found to contain other minor phases. PbTe, SnTe, and GeTe samples show good crystallinity structure and agree with the database. For the GeTe, the beaks are in good agreement with the standard PDF card of JCPDS#01-077-3540. In the case of PbTe, the peaks match the peak position from the standard PDF card of JCPDS#00-038-1435. Finally, for the SnTe, the peaks match the standard PDF card of JCPDS#00-008-0487. The crystalline structure, space group, and lattice parameters for each sample are shown in Table 2.

### 4.2 Geant4 analysis

The results were analyzed by obtaining the net count (*N*) or the area under the peak (*A*) using ROOT software (see Fig. 3). To get the sample’s absorption, the simulation was performed with and without the alloys sample, and the peak area was calculated in both cases (*A*) and (*A*<sub>0</sub>), respectively, taking into account that the primary photons are fixed in both cases. At least 107 primary monoenergetic photons must be generated to get the lowest relative error in all simulated cases. The simulated MAC can be calculated according to the following equation:

$$MAC = - \frac{\ln(A/A_0)}{X_m} \tag{1}$$

where *X<sub>m</sub>* (g/cm<sup>2</sup>) is called the mass distance and equal the absorber’s thickness multiplied by alloys sample density, *A*<sub>0</sub> and *A* are the main beam and the penetrated beam, respectively.

The Geant4 MC code was used to simulate the mass attenuation coefficient (MAC) of the four alloy

**Table 2** Lattice parameters of CrTe, PbTe, SnTe, and GeTe along with the structure and space group

Sample	Crystalline structure	Space group	Lattice constants (Å)		
			<i>a</i>	<i>b</i>	<i>c</i>
CrTe	Hexagonal	P6 <sub>3</sub> /mmc(194)	3.9699	3.9699	1.5527
PbTe	Cubic	Fm-3 m(225)	6.4590	6.4590	6.4590
SnTe	Cubic	Fm-3 m(225)	6.3030	6.3030	6.3030
GeTn	Trigonal	R3m(160)	8.3280	8.3280	10.6900

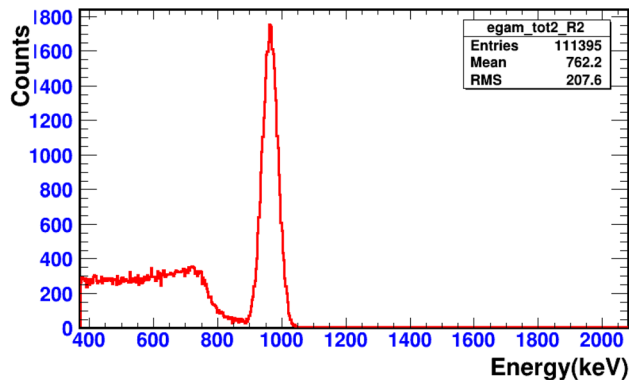


**Fig. 3** The simulated counts at 1000 keV and the obtained Peak from Root software

samples at energies between 0.015 and 15 MeV. Table 3 lists the results from Geant4, the XCOM program, and the corresponding relative differences. It is clear from this table that under the selected  $\gamma$ -ray energy, the simulated MAC results of the CrTe, GeTe, SnTe, and PbTe alloys are quite close to the theoretical results (i.e., XCOM code) at all energy regions. Therefore, the estimated MAC value of the alloys shows the same dependence on  $\gamma$ -ray energy. For instance, at first examine energy, the MAC for CrTe is 47.8 cm<sup>2</sup>/g (this is the Geant4 result), while the XCOM result is 47.9 cm<sup>2</sup>/g. At higher energy (1 MeV as an example) and for PbTe alloy, the Geant4 and XCOM values are 0.0638 and 0.0632 cm<sup>2</sup>/g. In the SnTe alloy, the simulated value is 0.0357 cm<sup>2</sup>/g, close to the 0.0351 cm<sup>2</sup>/g generated by XCOM. The relative deviation  $\Delta$  (%) between Geant4 and XCOM values are computed using Eq. (2):

$$(\Delta\%) = \frac{\text{MAC}_{\text{Geant4}} - \text{MAC}_{\text{XCOM}}}{\text{MAC}_{\text{XCOM}}} \times 100 \quad (2)$$

In Table 3, one can notice that for the four CrTe, GeTe, SnTe, and PbTe, the  $\Delta$  (%) is less than 2%, correct at all energies. This small  $\Delta$  (%) confirms the accuracy in the input file used in the current investigation. It emphasizes that the adopted method used

to evaluate MAC for the four prepared alloys can give accurate data.

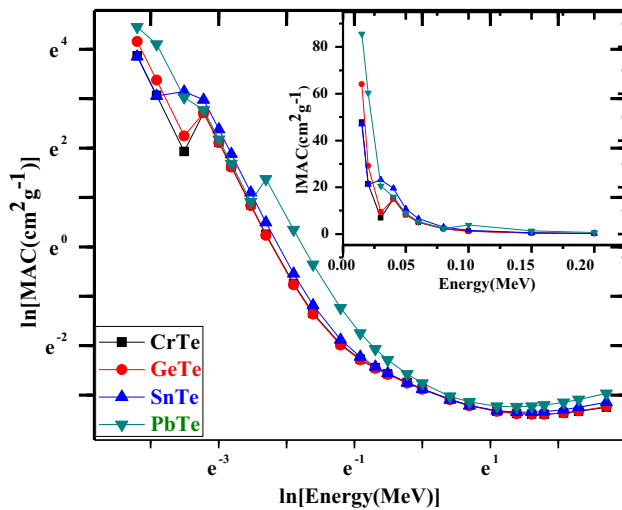
Figure 4 shows the relation between the MAC for the four alloys, and the photon energy ranged between 0.015 and 15 MeV. The MAC curve showed that the PbTe alloy has a better attenuation performance than CrTe, GeTe, and SnTe at all different energies. However, the SnTe alloy has the highest MAC values from 30 slightly up to 70 keV. The high MAC for SnTe alloy between 30 and 70 keV is attributed to Te. Sn elements have K-edge approximately at the same energy (31.8 and 29.2 keV, respectively), which leads to high absorption in this region. The MAC varied between 47.9 and 86.6 cm<sup>2</sup>/g at the lowest energy and then decreased until it reaches the value of the K-edge of the Te element, where it increases in the vacancy of the K-edge. After that, the MAC decreases quickly with increasing the energy. The curve takes the ordinary behavior according to the dominant interaction (photoelectric effect at low energy, Compton scattering at medium energy, and pair production at high energy). Due to the high atomic number of the lead, we can see that the PbTe alloy has the highest MAC value among the investigated alloys.

Figure 5 shows the relation between the linear attenuation coefficient (LAC) for the four alloys and the photon energy range from 0.015 to 15 MeV. As noticed in this figure, the LAC decreases with increasing energy; the current curve shows that the PbTe alloy has the highest LAC compared with the other alloys because it has a higher density except at low energy from 30–70 keV. The SnTe alloy has almost the same LAC despite having a density lower than the PbTe alloy. In the case of GeTe alloy, the maximum LAC occurred at the lowest energy (equals 304 cm<sup>-1</sup>). Then, it decreases with increasing energy up to 30 keV (on the vacancy of the K-edge of Te). It decreases quickly until 6 MeV, after this energy from 6 up to 15 MeV, the LAC increases with increasing the energy (where at 6 MeV, the LAC is 0.16 cm<sup>-1</sup>



**Table 3** The mass attenuation coefficient for the prepared alloys simulated by Geant4 code and calculated by XCOM software

Energy (MeV)	CrTe			GeTe			SnTe			PbTe		
	Geant4	XCOM	Δ%	Geant4	XCOM	Δ%	Geant4	XCOM	Δ%	Geant4	XCOM	Δ%
	1.50E-02	4.78E+01	4.79E+01	-0.25	6.33E+01	6.41E+01	-1.20	4.65E+01	4.70E+01	-1.24	8.66E+01	8.57E+01
2.00E-02	2.16E+01	2.15E+01	0.52	2.92E+01	2.92E+01	0.18	2.14E+01	2.12E+01	0.76	6.08E+01	6.05E+01	0.63
3.00E-02	6.89E+00	6.89E+00	0.01	9.53E+00	9.46E+00	0.82	2.34E+01	2.33E+01	0.59	2.05E+01	2.06E+01	-0.49
4.00E-02	1.51E+01	1.51E+01	0.11	1.50E+01	1.50E+01	-0.44	1.95E+01	1.96E+01	-0.46	1.61E+01	1.60E+01	0.38
5.00E-02	8.40E+00	8.32E+00	0.90	8.31E+00	8.24E+00	0.88	1.09E+01	1.08E+01	0.98	8.88E+00	8.81E+00	0.81
6.00E-02	5.06E+00	5.09E+00	-0.42	5.03E+00	5.02E+00	0.13	6.61E+00	6.57E+00	0.61	5.42E+00	5.39E+00	0.51
8.00E-02	2.35E+00	2.33E+00	0.85	2.26E+00	2.30E+00	-1.69	3.01E+00	3.00E+00	0.26	2.48E+00	2.49E+00	-0.22
1.00E-01	1.30E+00	1.29E+00	1.01	1.28E+00	1.27E+00	1.35	1.66E+00	1.64E+00	0.94	3.98E+00	3.95E+00	0.78
1.50E-01	4.75E-01	4.74E-01	0.21	4.70E-01	4.64E-01	1.23	5.77E-01	5.81E-01	-0.76	1.42E+00	1.41E+00	0.64
2.00E-01	2.59E-01	2.60E-01	-0.54	2.57E-01	2.55E-01	0.58	3.07E-01	3.06E-01	0.37	6.97E-01	6.99E-01	-0.31
3.00E-01	1.40E-01	1.39E-01	0.41	1.36E-01	1.37E-01	-0.46	1.53E-01	1.53E-01	0.44	2.91E-01	2.90E-01	0.36
4.00E-01	1.04E-01	1.03E-01	0.88	1.03E-01	1.02E-01	0.98	1.08E-01	1.08E-01	-0.29	1.75E-01	1.74E-01	0.24
5.00E-01	8.67E-02	8.62E-02	0.55	8.57E-02	8.51E-02	0.61	8.93E-02	8.85E-02	0.94	1.27E-01	1.26E-01	0.78
6.00E-01	7.63E-02	7.62E-02	0.22	7.55E-02	7.53E-02	0.28	7.69E-02	7.72E-02	-0.29	1.01E-01	1.01E-01	-0.24
8.00E-01	6.48E-02	6.40E-02	1.20	6.37E-02	6.34E-02	0.58	6.46E-02	6.40E-02	0.97	7.68E-02	7.62E-02	0.81
1.00E+00	5.63E-02	5.64E-02	-0.18	5.59E-02	5.59E-02	0.01	5.67E-02	5.61E-02	1.12	6.38E-02	6.32E-02	0.93
1.50E+00	4.60E-02	4.56E-02	0.82	4.53E-02	4.52E-02	0.12	4.55E-02	4.52E-02	0.77	4.88E-02	4.85E-02	0.64
2.00E+00	4.06E-02	4.04E-02	0.44	4.05E-02	4.01E-02	1.00	3.97E-02	4.03E-02	-1.28	4.37E-02	4.32E-02	1.07
3.00E+00	3.61E-02	3.58E-02	0.88	3.60E-02	3.57E-02	0.97	3.64E-02	3.63E-02	0.38	3.96E-02	3.97E-02	-0.32
4.00E+00	3.42E-02	3.41E-02	0.13	3.42E-02	3.41E-02	0.46	3.53E-02	3.52E-02	0.31	3.92E-02	3.92E-02	0.25
5.00E+00	3.33E-02	3.36E-02	-0.87	3.40E-02	3.37E-02	0.98	3.51E-02	3.51E-02	-0.10	3.97E-02	3.97E-02	0.08
6.00E+00	3.42E-02	3.36E-02	1.52	3.36E-02	3.38E-02	-0.61	3.57E-02	3.55E-02	0.50	4.04E-02	4.06E-02	-0.41
8.00E+00	3.49E-02	3.45E-02	1.22	3.48E-02	3.47E-02	0.24	3.73E-02	3.70E-02	0.76	4.32E-02	4.29E-02	0.63
1.00E+01	3.61E-02	3.57E-02	1.11	3.65E-02	3.60E-02	1.33	3.84E-02	3.88E-02	-0.97	4.58E-02	4.55E-02	0.81
1.50E+01	3.87E-02	3.89E-02	-0.52	3.95E-02	3.95E-02	0.20	4.32E-02	4.30E-02	0.31	5.12E-02	5.14E-02	-0.25



**Fig. 4** The mass attenuation coefficient as a function of the energy for the prepared alloys

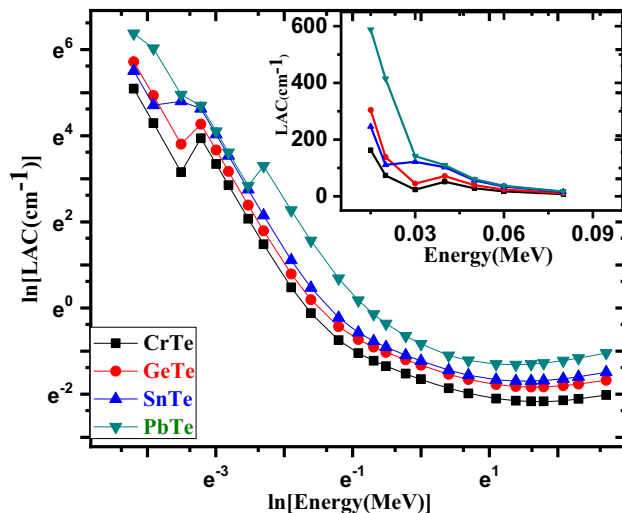


**Fig. 5** The linear attenuation coefficient as a function of the energy for the prepared alloys

while at 15 MeV, the LAC is  $0.19 \text{ cm}^{-1}$ ) that is due to the pair production where the nuclear field is dominant. We can notice that the variation between LAC and the energy can be classified into three main parts concerning the energy: the first part is below 0.03 MeV; in this part, the photoelectric effect is dominant, causing a quick reduction in the LAC [49]. The second part is at medium energy (between 0.03 and 6 MeV), where the Compton scattering phenomenon is dominant, causing the LAC of all four alloys to decrease with energy progressively. The last part takes place at higher energy; here, the pair production phenomenon is dominant, which leads to

increasing the LAC with energy. The influence of these three phenomena on the LAC is discussed in detail elsewhere [50, 51].

The variation of half and tenth value layers (HVL, TVL) values of the present alloys as a function of photon energies is presented in Figs. 6 and 7. According to these figures, SnTe has the lowest HVL value at the low energy from 30 up to 80 keV, while PbTe has the lowest HVL value between 0.08 MeV and 10 MeV. On the other hand, CrTe has the highest HVL and TVL values, ranging from 0.004 to 5.2 cm (for HVL) and (0.014 to 20.9 cm for TVL). These results imply that the higher the alloy density, the lower the HVL and TVL values, which indicates the effect of the density on the alloys shielding ability. This conclusion agrees with the findings obtained by Hamad et al., who practically measured the attenuation factors for  $\text{Fe}_x\text{Se}_{0.5}\text{Te}_{0.5}$  alloys and found that the  $\text{Fe}_{0.95}\text{Se}_{0.5}\text{Te}_{0.5}$  alloy with a density of  $5.836 \text{ g/cm}^3$  has the minimum HVL values [39].

The figures above demonstrate that all present alloy samples have small HVL and TVL values at low photon energies. For instance, the HVL is reported as 0.0042, 0.0023, 0.0028, and 0.0012 cm for CrTe, GeTe, SnTe and PbTe alloys respectively at 15 keV, while the TVL for the same alloys are 0.0141, 0.0076, 0.0093, and 0.0039 cm. This trend may be due to the advantage of the photoelectric effect in this region. We can conclude that a thin alloy sample is required for shielding the low-energy radiation. As the photon energy increases to the medium energy region, the

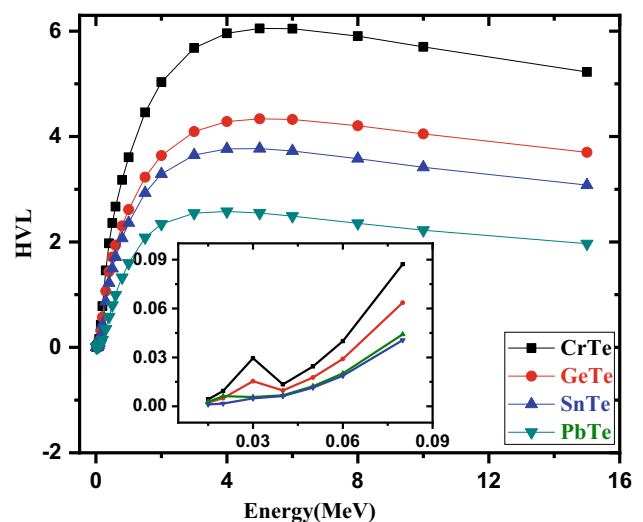


**Fig. 6** The half-value layer as a function of the energy for the prepared alloys

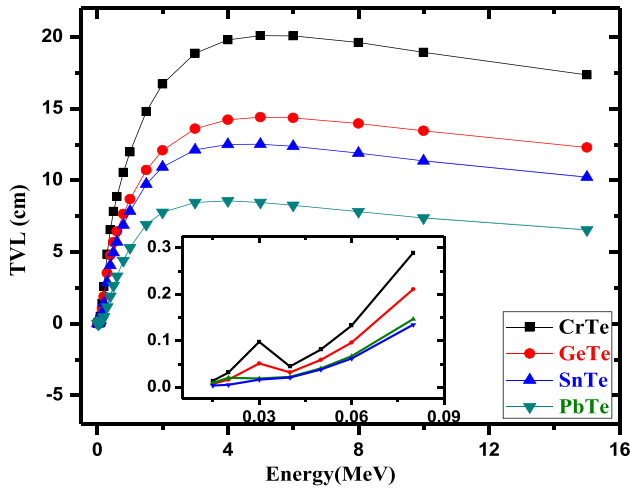


Fig. 7 The tenth value layer as a function of the energy for the prepared alloys

HVL and TVL values gradually increase. This trend in HVL and TVL occurs because of the dominance of Compton scattering. This implies that it is important to increase the alloys' dimension to enhance the shielding capability, especially if used in applications requiring relatively high energy. The slight increase in HVL values at higher energy can be attributed to the pair production process's dominance at these energies. At the last tested energy, HVL values are as follows: 5.23 cm, 3.70 cm, 3.07 cm, and 1.97 cm for CrTe, GeTe, SnTe, and PbTe, respectively. In the same energy range, TVL takes the following values: 17.36 cm, 12.29 cm, 10.23 cm, and 6.53 cm for CrTe, GeTe, SnTe, and PbTe, respectively. The densities are  $3.4075 \text{ g/cm}^3$  and  $6.8615 \text{ g/cm}^3$  for CrTe and PbTe, respectively. So, when the density is doubled, a reduction in the HVL by a factor of 2.65 is found at 15 MeV, while a reduction of TVL by a factor of 1.88 is found at the same energy. At moderate energy (say 1 MeV), a reduction by a factor of 2.27 and 2.25 is found in HVL and TVL, respectively, due to the enhancement of the density from  $3.4075 \text{ g/cm}^3$  to  $6.8615 \text{ g/cm}^3$ .

The prepared alloys' effective atomic number ( $Z_{\text{eff}}$ ) was evaluated from the Phy-X software [45]. The obtained results are shown in Fig. 8. The  $Z_{\text{eff}}$  of PbTe is higher than that of other alloys. This high value is mainly due to lead (Pb) content, with a high atomic number (82). Similarly, the  $Z_{\text{eff}}$  of CrTe and GeTe is nearly the same at low energy, but for  $E > 100 \text{ keV}$ , the CrTe alloy has the lowest  $Z_{\text{eff}}$  compared with present alloys. From the figure, the  $Z_{\text{eff}}$  of all the

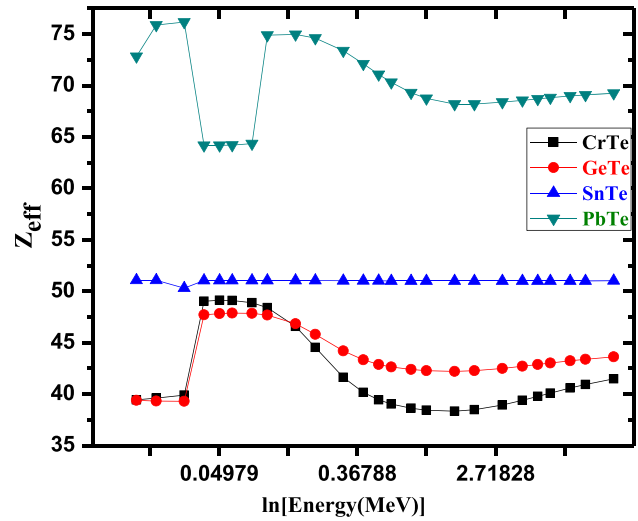


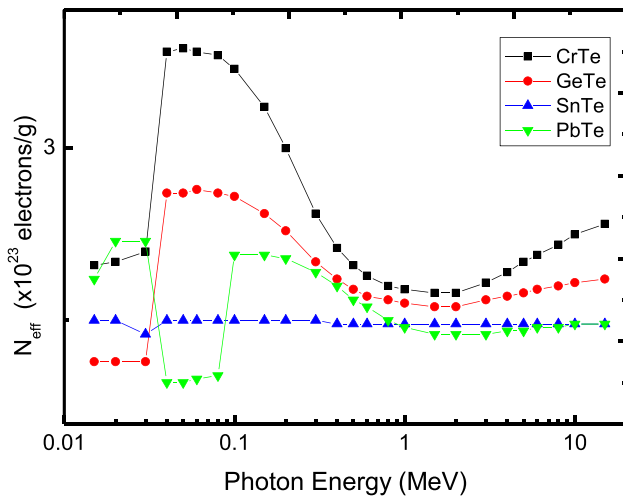
Fig. 8 The effective atomic number as a function of the energy for the prepared alloys

studied alloys changes with increasing the energy, except for SnTe, which is relatively constant with energy. The constancy in the  $Z_{\text{eff}}$  for SnTe can be explained according to the atomic number of Sn and Te. These two elements have a close atomic number (50 for Sn and 52 for Te), which explains  $Z_{\text{eff}}$ 's constancy. For instance, the  $Z_{\text{eff}}$  values are 51.06 at 15 keV, 50.33 at 30 keV, 51.04 at 0.2 MeV, 51.00 at 1 MeV and 51.01 at 15 MeV. It is found that the  $Z_{\text{eff}}$  is less than 52 and higher than 50 (between the atomic number of Sn and Te). This constancy in  $Z_{\text{eff}}$  matches the  $Z_{\text{eff}}$  values reported for Ag–Pd alloy [52]. For  $E > 100 \text{ keV}$ , the  $Z_{\text{eff}}$  follows the trend:  $\text{CrTe} < \text{GeTe} < \text{SnTe} < \text{PbTe}$ . PbTe has the greatest  $Z_{\text{eff}}$  at all energies. It is well known that  $Z_{\text{eff}}$  directly correlates with radiation shielding ability, which explains why the PbTe alloys prove to have superior protection potential. Electron density ( $N_{\text{eff}}$ ) is another parameter that can be used to describe the materials characterization. The electron density can be determined from the linear attenuation coefficient (LAC) values.

Figure 9 shows the electron density ( $N_{\text{eff}}$ ) of all-alloy samples. From Fig. 9, it is obvious that CrTe (lowest density) owns the highest electron density, followed by GeTe. The CrTe and GeTe samples have the same trends at all energy, while the behavior for SnTe and PbTe is completely different due to the difference in elements in each alloy.

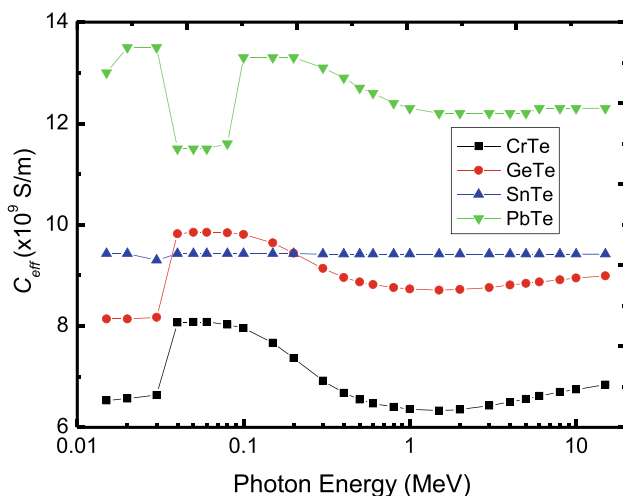
The number of unbound electrons inside the substance may be changed according to different types of interaction between photons and materials. This



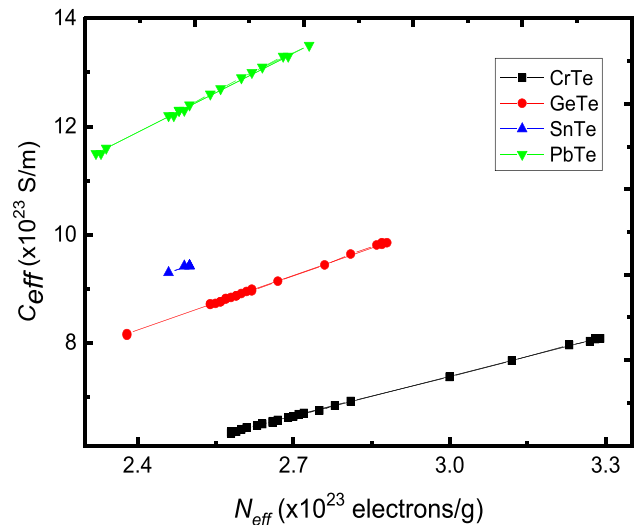


**Fig. 9** The electron density as a function of the energy for the prepared alloys

variation in unbound electron numbers can affect electron density (effective electron number) in the substance. So, increasing the photon energy can lead to a change in electrical conductivity ( $C_{eff}$ ) of the substances depending on electron density. In this work, we present the  $C_{eff}$  in Fig. 10. We note from Fig. 10 that the PbTe has the highest  $C_{eff}$  within all the energy ranges, followed by SnTe, GeTe, and CrTe, respectively. This behavior is related to alloy samples' density values and electron density, as listed in Table 1. The density values are 6.862, 5.232, 4.747, and 3.408 g/cm<sup>3</sup> for PbTe, SnTe, GeTe, and CrTe. The relation between  $N_{eff}$  and  $C_{eff}$  is presented in Fig. 11.



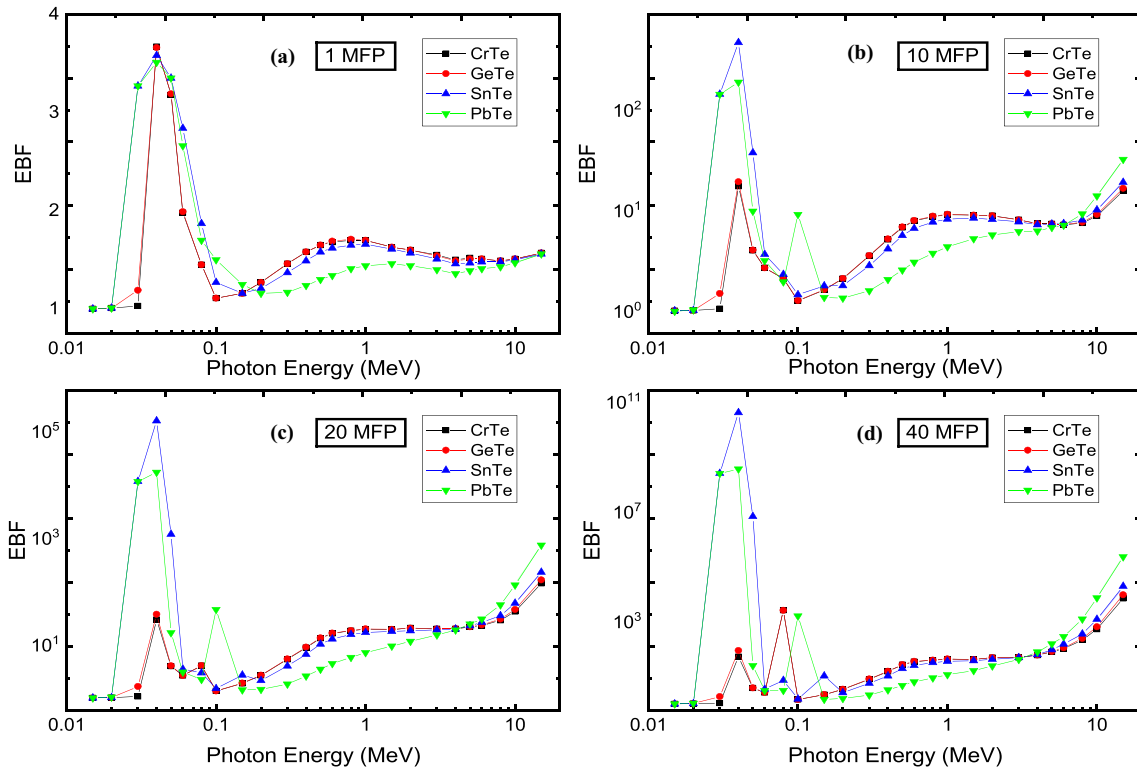
**Fig. 10** The electrical conductivity as a function of the energy for the prepared alloys



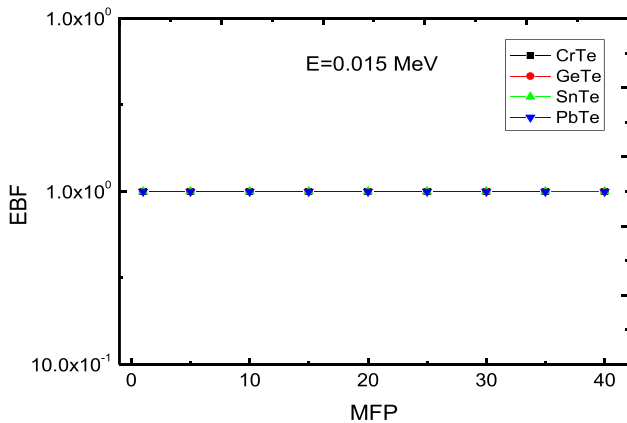
**Fig. 11** The relation between the electron density and electrical conductivity

The figure shows the same behavior for  $C_{eff}$  and  $N_{eff}$  with energy.

Figure 12 presents the prepared alloys' exposure buildup factor (EBF) at 1, 10, 20, and 40 mfp. The trend in the EBF for the four alloys is similar at the four investigated penetration depths. At the first two energies, the four alloys show almost the same EBF values, and this is clearly seen in Fig. 13, where we plotted the EBF for the tested alloys at 0.015 MeV to confirm that the different alloys have almost the same EBF values at this energy (around 1). As shown from Fig. 12, at low energy, a peak in EBF is observed, which occurs at 30 keV, near the K absorption edge of Te. Also, we can see another small peak observed for PbTe alloy at around 0.1 MeV. Moreover, the observed peak for SnTe and PbTe is sharper than that for CrTe and GeTe. For  $E > 0.1$  MeV, the EBF increases with energy. The EBF values for PbTe alloy (representing the green triangle) are lower than those of CrTe, GeTe, and SnTe. This is correct for  $E < 10$  MeV. The data in Fig. 12 also shows that the EBF curves have a Gaussian distribution shape in the moderate energy range, with a maximum value in average energy at about 1 MeV in Fig. 12 a and b. While, in Fig. 12c and d, we can see that the EBF attains the maximum values for  $E > 8$  MeV. One can see that the EBF values given in Fig. 12d are higher than those given in Fig. 12a–c, while the lowest values are reported at 1 MFP. This trend suggests that increasing the penetration depth is found to remarkably influence the EBF values.



**Fig. 12** The exposure buildup factor as a function of the energy for the prepared alloys



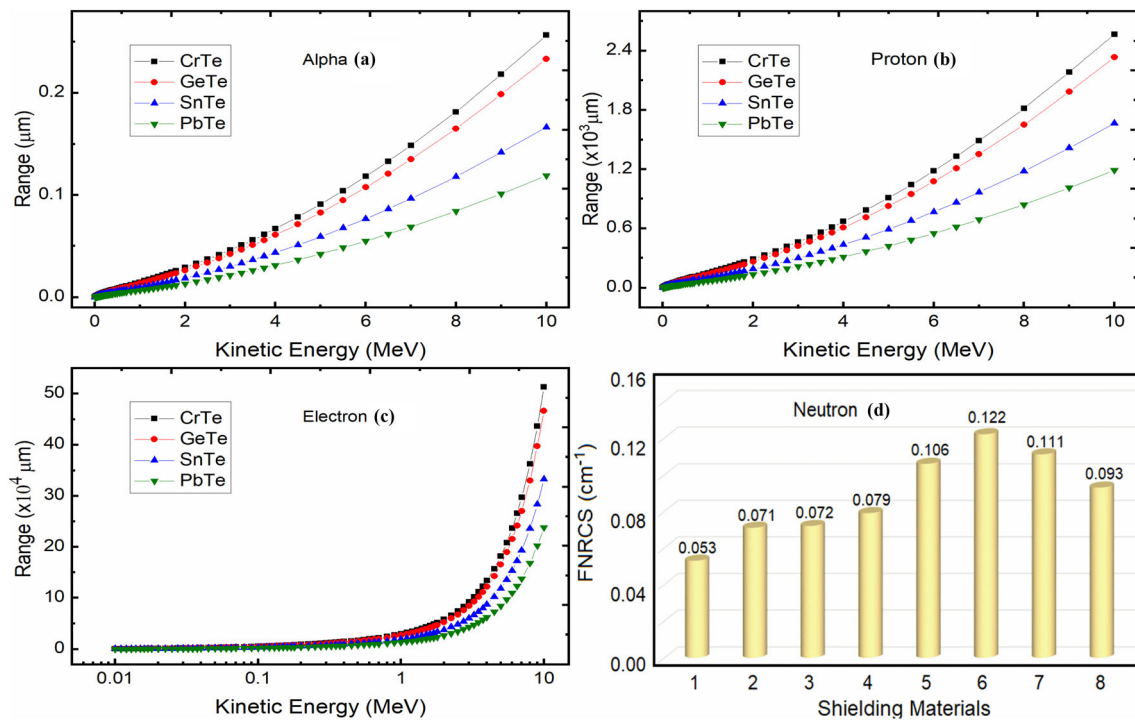
**Fig. 13** The exposure buildup factor as a function of the penetration depth at 0.015 MeV

Figure 14a, b, and c show the projected range for various charged particles like alpha, proton, and electron. The projected range represents the distance travel for charged particles inside the materials before depositing their energy. It is obvious that the electron has the highest projected range, then proton and an alpha particle. The project range depends on the mass and the charge of the particle. Here, the alpha particle has the highest mass and charge

compared with other charged particles, protons, and electrons. CrTe shows the highest projected range compared with GeTe, SnTe, and PbTe. This result is compatible with density for all samples. In contrast, the removal cross-section for fast neutron ( $\Sigma_R$ ) is represented in Fig. 14d. This parameter was determined via the Phy-X program. The  $\Sigma_R$  values for CrTe, GeTe, SnTe and PbTe are 0.053, 0.071, 0.072 and 0.079  $\text{cm}^{-1}$ , respectively. The  $\Sigma_R$  for prepared alloys were compared with ordinary concrete (OC), Basalt (BM), steel magnet (SM) concrete, and Graphene that have  $\Sigma_R$  values are 0.106, 0.122, 0.111, and 0.093  $\text{cm}^{-1}$ , respectively. The  $\Sigma_R$  for alloy samples was lower than the other samples.

### 5 Conclusion

Four Te-based alloy samples were prepared and studied for possible use in radiation shielding applications. The XRD results reveal a second phase for CrTe, while a single phase is obtained in the rest of the samples (PbTe, SnTe, and GeTe). The alloy samples' densities are 3.4075, 4.7478, 5.2323, and 6.8615  $\text{g}/\text{cm}^3$  for CrTe, GeTe, SnTe, and PbTe,



**Fig. 14** The projected range for (a) alpha (b) proto (c) electron and (d) fast neutron removal cross-section for all alloy samples

respectively. The density values gave us a good indication for the sample that has superior radiation shielding properties. Two programs (Geant4 and XCOM) were utilized to determine the MAC; the relative deviation between these programs' values is very low. The SnTe showed the lowest HVL results within the energy range from 30 to 80 keV; after this range, the PbTe displays the lowest HVL at energy  $E > 100$  MeV. The  $Z_{\text{eff}}$  value for the PbTe alloy was higher than other samples due to the higher atomic number for Te and Pb. The EBF values showed the same behavior for all samples, while the EBF values were the same for all samples at 0.015 MeV. The projected range for the CrTe was the highest for all charged particles, while the PbTe showed the highest  $\Sigma_R$ . Based on the obtained results, we conclude that the PbTe has superior shielding properties for photons, neutrons, and charged particles. So PbTe can be used as a radiation shielding substance.

## Acknowledgements

Authors from KFUPM acknowledge the support provided by the Deanship of Scientific Research at King Fahd University of Petroleum & Minerals (KFUPM) for funding this work.

## Declarations

**Conflict of interest** The authors declare that they have no known competing financial interests or personal relationships that could have appeared to influence the work reported in this paper.

## References

1. B. Aygün, E. Şakar, T. Korkut, M.I. Sayyed, A. Karabulut, New high-temperature resistant heavy concretes for fast neutron and gamma radiation shielding. *Radiochim. Acta* **107**, 359–367 (2019). <https://doi.org/10.1515/ract-2018-3075>
2. I. Akkurt, C. Basyigit, S. Kilincarslan, B. Mavi, A. Akkurt, Radiation shielding of concretes containing different aggregates. *Cem. Concr. Compos.* **28**, 153–157 (2006). <https://doi.org/10.1016/j.cemconcomp.2005.09.006>
3. I.I. Bashter, Calculation of radiation attenuation coefficients for shielding concretes. *Ann. Nucl. Energy* **24**, 1389–1401 (1997). [https://doi.org/10.1016/S0306-4549\(97\)00003-0](https://doi.org/10.1016/S0306-4549(97)00003-0)
4. A.V. Trukhanov, S.S. Grabchikov, A.A. Solobai, D.I. Tishkevich, S.V. Trukhanov, E.L. Trukhanova, AC and DC-shielding properties for the Ni80Fe20/Cu film structures. *J. Magn. Magn. Mater.* **443**, 142–148 (2017). <https://doi.org/10.1016/j.jmmm.2017.07.053>

5. D.I. Tishkevich, S.S. Grabchikov, S.B. Lastovskii, S.V. Trukhanov, T.I. Zubar, D.S. Vasin, A.V. Trukhanov, A.L. Kozlovskiy, M.M. Zdorovets, Effect of the synthesis conditions and microstructure for highly effective electron shields production based on Bi coatings. *ACS Appl. Energy Mater.* **1**, 1695–1702 (2018). <https://doi.org/10.1021/acsaem.8b00179>
6. D.I. Tishkevich, S.S. Grabchikov, S.B. Lastovskii, S.V. Trukhanov, D.S. Vasin, T.I. Zubar, A.L. Kozlovskiy, M.V. Zdorovets, V.A. Sivakov, A.V. Muradyan, T.R. Trukhanov, Function composites materials for shielding applications: Correlation between phase separation and attenuation properties. *J. Alloys Compd.* **771**, 238–245 (2019). <https://doi.org/10.1016/j.jallcom.2018.08.209>
7. A.H. Abdalsalam, M.I. Sayyed, T. Ali Hussein, E. Şakar, M.H.A. Mhareb, B. Ceviz Şakar, B. Alim, K.M. Kaky, A study of gamma attenuation property of UHMWPE/Bi<sub>2</sub>O<sub>3</sub> nanocomposites. *Chem. Phys.* **523**, 92–98 (2019). <https://doi.org/10.1016/j.chemphys.2019.04.013>
8. A.H. Abdalsalam, E. Şakar, K.M. Kaky, M.H.A. Mhareb, B. Ceviz Sakar, M.I. Sayyed, A. Gürol, Investigation of gamma ray attenuation features of bismuth oxide nano powder reinforced high-density polyethylene matrix composites. *Eur. Phys. J. Plus* **168**, 108537 (2020). <https://doi.org/10.1016/j.radphyschem.2019.108537>
9. M.H.A. Mhareb, M.I. Sayyed, Y.S.M. Alajerami, M. Alqahtani, N. Dwaikat, A.M. Alsagry, M. Al-Yatimi, M. Zakariah, Structural and radiation shielding features for a new series of borate glass samples: part I. *Eur. Phys. J. Plus* (2021). <https://doi.org/10.1140/epjp/s13360-020-00984-7>
10. M.I. Sayyed, A.A. Ati, M.H.A. Mhareb, K.A. Mahmoud, K.M. Kaky, S.O. Baki, M.A. Mahdi, Novel tellurite glass (60-x)TeO<sub>2</sub>-10GeO<sub>2</sub>-20ZnO-10BaO-xBi<sub>2</sub>O<sub>3</sub> for radiation shielding. *J. Alloys Compd.* **844**, 155668 (2020). <https://doi.org/10.1016/j.jallcom.2020.155668>
11. M. Monisha, A.N. D'Souza, V. Hegde, N.S. Prabhu, M.I. Sayyed, G. Lakshminarayana, S.D. Kamath, Dy<sup>3+</sup> doped SiO<sub>2</sub>-B<sub>2</sub>O<sub>3</sub>-Al<sub>2</sub>O<sub>3</sub>-NaF-ZnF<sub>2</sub> glasses: an exploration of optical and gamma radiation shielding features. *Curr. Appl. Phys.* **20**, 1207–1216 (2020). <https://doi.org/10.1016/j.cap.2020.08.004>
12. M.H.A. Mhareb, M. Alqahtani, F. Alshahri, Y.S.M. Alajerami, N. Saleh, N. Alonizan, M.I. Sayyed, M.G.B. Ashiq, T. Ghrib, S.I. Al-Dhafar, T. Alayed, M.A. Morsy, The impact of barium oxide on physical, structural, optical, and shielding features of sodium zinc borate glass. *J. Non-Cryst. Solids.* **541**, 120090 (2020). <https://doi.org/10.1016/j.jnoncrysol.2020.120090>
13. Y. Alajerami, D. Drabold, M. Mhareb, K. Subedi, K. Cimat, G. Chen, Physical, structural, and shielding properties of cadmium bismuth borate-based glasses. *J. Appl. Phys.* (2020). <https://doi.org/10.1063/1.5143116>
14. M.K. Hamad, M.H.A. Mhareb, Y.S. Alajerami, M.I. Sayyed, G. Saleh, Y. Maswadeh, K.A. Ziq, Radiation shielding properties of Nd<sub>0.6</sub>Sr<sub>0.4</sub>Mn<sub>1-y</sub>Ni<sub>y</sub>O<sub>3</sub> substitute with different concentrations of nickle. *Radiat. Phys. Chem.* (2020). <https://doi.org/10.1016/j.radphyschem.2020.108920>
15. F. Akman, Z.Y. Khattari, M.R. Kaçal, M.I. Sayyed, F. Afaneh, The radiation shielding features for some silicide, boride and oxide types ceramics. *Radiat. Phys. Chem.* **160**, 9–14 (2019). <https://doi.org/10.1016/j.radphyschem.2019.03.001>
16. M.H.A. Mhareb, Y. Slimani, Y.S. Alajerami, M.I. Sayyed, E. Lacomme, M.A. Almessiere, Structural and radiation shielding properties of BaTiO<sub>3</sub> ceramic with different concentrations of Bismuth and Ytterbium. *Ceram. Int.* **46**, 28877–28886 (2020). <https://doi.org/10.1016/j.ceramint.2020.08.055>
17. D.I. Shlimas, M.V. Zdorovets, A.L. Kozlovskiy, Synthesis and resistance to helium swelling of Li<sub>2</sub>TiO<sub>3</sub> ceramics. *J. Mater. Sci. Mater. Electron.* **31**, 12903–12912 (2020). <https://doi.org/10.1007/s10854-020-03843-4>
18. M.V. Zdorovets, A.S. Kurlov, A.L. Kozlovskiy, Radiation defects upon irradiation with Kr<sup>14+</sup> ions of TaC<sub>0.81</sub> ceramics. *Surf. Coat. Technol.* **386**, 125499 (2020). <https://doi.org/10.1016/j.surfcoat.2020.125499>
19. M.V. Zdorovets, I.E. Kenzhina, V. Kudryashov, A.L. Kozlovskiy, Helium swelling in WO<sub>3</sub> microcomposites. *Ceram. Int.* **46**, 10521–10529 (2020). <https://doi.org/10.1016/j.ceramint.2020.01.053>
20. T. Kaur, J. Sharma, T. Singh, Review on scope of metallic alloys in gamma rays shield designing. *Prog. Nucl. Energy.* **113**, 95–113 (2019). <https://doi.org/10.1016/j.pnucene.2019.01.016>
21. K.S. Babu, S.C. Lingam, D.V. Krishna Reddy, Gamma-ray cross sections and effective atomic numbers in some alloys in the energy range 32 to 662 keV. *Can. J. Phys.* (1984). <https://doi.org/10.1139/p84-028>
22. D.V. KrishnaReddy, K.S. Babu, S.C. Lingam, Photon cross sections and effective atomic numbers in some alloys. *Can. J. Phys.* (1985). <https://doi.org/10.1139/p85-237>
23. P. Limkitjaroenporn, J. Kaewkhao, S. Asavavisithchai, Determination of mass attenuation coefficients and effective atomic numbers for Inconel 738 alloy for different energies obtained from Compton scattering. *Ann. Nucl. Energy* **53**, 64–68 (2013). <https://doi.org/10.1016/j.anucene.2012.08.020>
24. U. Perişanoğlu, L. Demir, A study of K shell X-ray intensity ratios of Ni<sub>x</sub>Cr<sub>1-x</sub> alloys in external magnetic field and determination of effective atomic numbers of these alloys. *Radiat. Phys. Chem.* **110**, 119–125 (2015). <https://doi.org/10.1016/j.radphyschem.2015.01.032>

25. R. Sharma, J. Sharma, T. Singh, Effective atomic numbers for some alloys at 662 keV using gamma rays backscattering technique. *Phys. Sci. Int. J.* **11**, 1–6 (2016). <https://doi.org/10.9734/psij/2016/27243>
26. S. Kaur, A. Kaur, P.S. Singh, T. Singh, Scope of Pb-Sn binary alloys as gamma rays shielding material. *Prog. Nucl. Energy* **93**, 277–286 (2016). <https://doi.org/10.1016/j.pnucene.2016.08.022>
27. S. Kobayashi, N. Hosoda, R. Takashima, Tungsten alloys as radiation protection materials. *Nucl. Instruments Methods Phys. Res. Sect. A* **390**, 426–430 (1997). [https://doi.org/10.1016/S0168-9002\(97\)00392-6](https://doi.org/10.1016/S0168-9002(97)00392-6)
28. N. Jamal AbuAlRoos, M.N. Azman, N.A. Baharul Amin, R. Zainon, Tungsten-based material as promising new lead-free gamma radiation shielding material in nuclear medicine. *Phys. Med.* **78**, 48–57 (2020). <https://doi.org/10.1016/j.ejmp.2020.08.017>
29. V.R.K. Murty, D.P. Winkoun, K.R.S. Devan, Effective atomic numbers for W/Cu alloy using transmission experiments. *Appl. Radiat. Isot.* **53**, 945–948 (2000). [https://doi.org/10.1016/S0969-8043\(00\)00248-7](https://doi.org/10.1016/S0969-8043(00)00248-7)
30. V.R.K. Murty, Effective atomic numbers for W/Cu alloy for total photon attenuation. *Radiat. Phys. Chem.* **71**, 667–669 (2004). <https://doi.org/10.1016/j.radphyschem.2004.04.046>
31. S. Seven, I.H. Karahan, Ö.F. Bakkaloglu, The measurement of total mass attenuation coefficients of CoCuNi alloys. *J. Quant. Spectrosc. Radiat. Transf.* **83**, 237–242 (2004). [https://doi.org/10.1016/S0022-4073\(03\)00118-3](https://doi.org/10.1016/S0022-4073(03)00118-3)
32. O. Jelli, S. Erzeneoğlu, I.H. Karahan, G. Çankaya, Effective atomic numbers for CoCuNi alloys using transmission experiments. *J. Quant. Spectrosc. Radiat. Transf.* **91**, 485–491. (2005). <https://doi.org/10.1016/j.jqsrt.2004.07.006>
33. G. Apaydin, E. Cengiz, E. Tirasoğlu, V. Aylikci, F.O. Bakkaloğlu, Studies on mass attenuation coefficients, effective atomic numbers and electron densities for CoCuAg alloy thin film. *Phys. Scr.* (2009). <https://doi.org/10.1088/0031-8949/79/05/055302>
34. J. Kaewkhao, J. Laopaiboon, W. Chewpraditkul, Determination of effective atomic numbers and effective electron densities for Cu/Zn alloy. *J. Quant. Spectrosc. Radiat. Transf.* **109**, 1260–1265 (2008). <https://doi.org/10.1016/j.jqsrt.2007.10.007>
35. V.P. Singh, N.M. Badiger, Study of mass attenuation coefficients, effective atomic numbers and electron densities of carbon steel and stainless steels. *Radioprotection* **48**, 431–443 (2013). <https://doi.org/10.1051/radiopro/2013067>
36. J. Blink, J. Farmer, J. Choi, C. Saw, Applications in the nuclear industry for thermal spray amorphous metal and ceramic coatings. *Metall. Mater. Trans. A* **40**, 1344–1354 (2009). <https://doi.org/10.1007/s11661-009-9830-4>
37. S. M. Al-Jaff, Investigation the Effective atomic number , electron density, Half value layer and mean free path of steel types 304 and 347 in the energy range 40KeV-130KeV, *Journal of Natural Sciences Research.* **5** (2013). ISSN 2225-0921. <https://www.iiste.org/Journals/index.php/JNSR/article/view/9723>.
38. R. Singh, S. Singh, G. Singh, K. Singh, Gamma radiation shielding properties of steel and iron slags. *Sci. Res.* (2017). <https://doi.org/10.4236/njgc.2017.71001>
39. R.M. Hamad, M.H.A. Mhareb, Y.S. Alajerami, M.I. Sayyed, G. Saleh, M.K. Hamad, K.A. Ziq, A comprehensive ionizing radiation shielding study of Fe<sub>x</sub>Se<sub>0.5</sub>Te<sub>0.5</sub> alloys with various iron concentrations. *J. Alloys Compd.* (2020). <https://doi.org/10.1016/j.jallcom.2020.157636>
40. M.K. Hamad, E. Martinez-Teran, Y. Maswadeh, R. Hamad, E.G. Al-Nahari, A.A. El-Gendy, K.A. Ziq, Room temperature magnetocaloric effect in CrTe<sub>1-x</sub>Sb<sub>x</sub> alloys. *J. Magn. Magn. Mater.* **514**, 167171 (2020). <https://doi.org/10.1016/j.jmmm.2020.167171>
41. M.K. Hamad, K.A. Ziq, Critical behavior of CrTe<sub>1-x</sub>Sb<sub>x</sub> ferromagnet. *AIP Adv.* (2018). <https://doi.org/10.1063/1.5042550>
42. M.K. Hamad, Y. Maswadeh, E. Martinez-Teran, A. El-Gendy, K. Ziq, Structural, magnetic, and critical behavior of CrTe<sub>1-x</sub>Sb<sub>x</sub> alloys. *Eur. Phys. J. Plus* (2021). <https://doi.org/10.1140/epjp/s13360-021-01534-5>
43. B.O. Soederberg, E. Zeppezauer, T. Boive, B.N. And, C. Brändén, Structure of Horse Liver Alcohol Dehydrogenase. II. Heavy-atom Derivatives of Type A Crystals., **24** (1970) 3567–3574. <https://doi.org/10.3891/acta.chem.scand.24-3567>.
44. L. Gerward, N. Guilbert, K.B. Jensen, H. Levring, WinX-Com—a program for calculating X-ray attenuation coefficients. *Radiat. Phys. Chem.* **71**, 653–654 (2004). <https://doi.org/10.1016/j.radphyschem.2004.04.040>
45. E. Şakar, Ö.F. Özpolat, B. Alim, M.I. Sayyed, M. Kurudirek, Phy-X/PSD: Development of a user friendly online software for calculation of parameters relevant to radiation shielding and dosimetry. *Radiat. Phys. Chem.* (2020). <https://doi.org/10.1016/j.radphyschem.2019.108496>
46. P. Rodrigues, A. Trindade, L. Peralta, C. Alves, A. Chaves, M. Lopes, Application of GEANT4 radiation transport toolkit to dose calculations in anthropomorphic phantoms. *Appl. Radiat. Isot.* **61**, 1451–1461 (2004). <https://doi.org/10.1016/j.apradiso.2004.05.073>
47. M. Hamad, Bragg-curve simulation of carbon-ion beams for particle-therapy applications: a study with the GEANT4 toolkit. *Nucl. Eng. Technol.* **53**, 2767–2773 (2021). <https://doi.org/10.1016/j.net.2021.02.011>



48. G.B. Street, E. Sawatzky, K. Lee, Magnetic properties of vapor grown crystals of hexagonal chromium telluride. *J. Phys. Chem. Solids*. **34**, 1453–1455 (1973). [https://doi.org/10.1016/S0022-3697\(73\)80048-4](https://doi.org/10.1016/S0022-3697(73)80048-4)
49. Y. Al-Hadeethi, M.I. Sayyed, BaO–Li<sub>2</sub>O–B<sub>2</sub>O<sub>3</sub> glass systems: Potential utilization in gamma radiation protection. *Prog. Nucl. Energy*. **129**, 103511 (2020). <https://doi.org/10.1016/j.pnucene.2020.103511>
50. M.I. Sayyed, Y. Al-Hadeethi, M.M. AlShammari, M. Ahmed, S.H. Al-Heniti, Y.S. Rammah, Physical, optical and gamma radiation shielding competence of newly boro-tellurite based glasses: TeO<sub>2</sub>–B<sub>2</sub>O<sub>3</sub>–ZnO–Li<sub>2</sub>O<sub>3</sub>–Bi<sub>2</sub>O<sub>3</sub>. *Ceram. Int*. **47**, 611–618 (2020). <https://doi.org/10.1016/j.ceramint.2020.08.168>
51. N. Chanthima, J. Kaewkhao, Investigation on radiation shielding parameters of bismuth borosilicate glass from 1 keV to 100 GeV. *Ann. Nucl. Energy*. **55**, 23–28 (2013). <https://doi.org/10.1016/j.anucene.2012.12.011>
52. O. Agar, M.I. Sayyed, F. Akman, H.O. Tekin, M.R. Kaçal, An extensive investigation on gamma ray shielding features of Pd/Ag-based alloys. *Nucl. Eng. Technol*. **51**, 853–859 (2019). <https://doi.org/10.1016/j.net.2018.12.014>

**Publisher's Note** Springer Nature remains neutral with regard to jurisdictional claims in published maps and institutional affiliations.